22nd International Conference on Renewable Energies and Power Quality (ICREPQ'24)
Bilbao (Spain), 26th to 28th June 2024

ISBN: 978-84-09-60656-6

Ripple current control for single phase-shift dual active bridge converters

Sz. Veréb, L. Stranyóczky, Z. Sütő and A. Balogh

Department of Automation and Applied Informatics
Faculty of Electrical Engineering and Informatics
Budapest University of Technology and Economics
Műegyetem rkp. 3., H-1111 Budapest (Hungary)
Phone number: +36 (1) 463-1552

Abstract. Nowadays, the need for isolated bidirectional DC/DC converters is growing. In these types of equipment, the dual active bridge topology is widespread, where mostly the transformer leakage inductance value determines its dynamic behavior. Voltage imbalance between the primary and secondary side results in unwanted excessive transformer peak current if the leakage inductance is low, thus limiting the load transient response of the converter. In this paper, a ripple current control method is presented, which reduces the transformer peak current to its minimal level, furthermore, allows the magnetizing current components to be distributed between the primary and secondary sides in an arbitrary proportion. The proposed control was tested in HIL simulation and on a real 360 kW dual active bridge converter. Based on the results the current stress on semiconductors and DC capacitors were reduced while the utilization and the efficiency of the converter were increased.

Key words. dual active bridge, ripple current, single phase-shift, converter

1. Introduction

Nowadays, the need for bidirectional isolated DC/DC converters is growing as electric energy storage is becoming more widespread [1]. The most common converter topology in such types of equipment is the dual active bridge (DAB) [2–4], which was first published and patented in 1991 [5, 6]. The main circuit consists of a transformer and two actively driven MOSFET or IGBT-based full bridge inverter blocks, as shown in Figure 1 (a). The L_{sp} and L_{ss} leakage inductances of the transformer are the key elements in the converter operation [7].

The single phase-shift (SPS) control is the most commonly used method due to its simplicity [7], despite its disadvantageous properties such as backflow power, high peak current, and narrow zero voltage switching (ZVS) region [8]. In recent years various control and modulation techniques were published to mitigate these adverse effects, such as the dual phase-shift (DPS) [9] and triple phase-shift (TPS) [10] methods. However, such solutions may become difficult to implement in practical applications due to their higher degrees of freedom in control parameters [8].

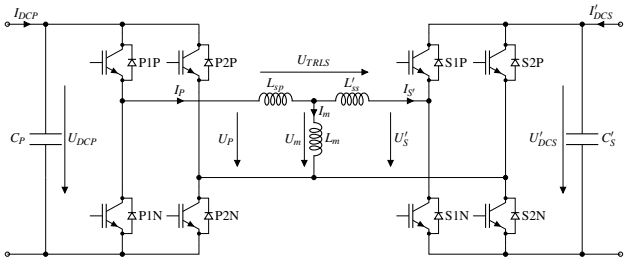

Fig. 1. DAB converter power circuit schematic.

Most recent papers are focusing on the improvement of converter efficiency [11, 12] and the reduction of physical size by operating with high switching frequency [13, 14].

In most applications, the load transient response of the DAB converter is crucial as unexpected events may occur such as load dump or short circuit. To prevent the DC voltages from over- or undershooting in such conditions, a capacitor bank with higher total capacitance can be used which increases the equipment cost. Another option is to use a transformer with a low leakage inductance value resulting in a higher current rate of change [15]. By decreasing the leakage inductance, the primary and secondary side voltage difference becomes more significant.

Using the SPS control technique, U'_{DCS} is regulated by the I'_S transformer current, which is controlled by the voltage-time product applied onto the transformer leakage inductance (see t_{SPS} in Figure 2 (a)). Usually, a cascaded control architecture is applied, where the outer U'_{DCS} voltage control loop provides the reference for the inner I'_S current controller. A few volts of difference between the primary and the secondary side voltage may result in an unwanted ripple current in addition to the transformer's inevitable magnetizing current (as shown in Figure 2 (c)), causing high current stress on the main circuit elements and increased power loss. Considering these side effects, it would theoretically be a preferable choice to set the U'_{DCS} reference equal to U_{DCP}. However, in practical applications, this is not an ideal solution due to voltage measurement imperfections.

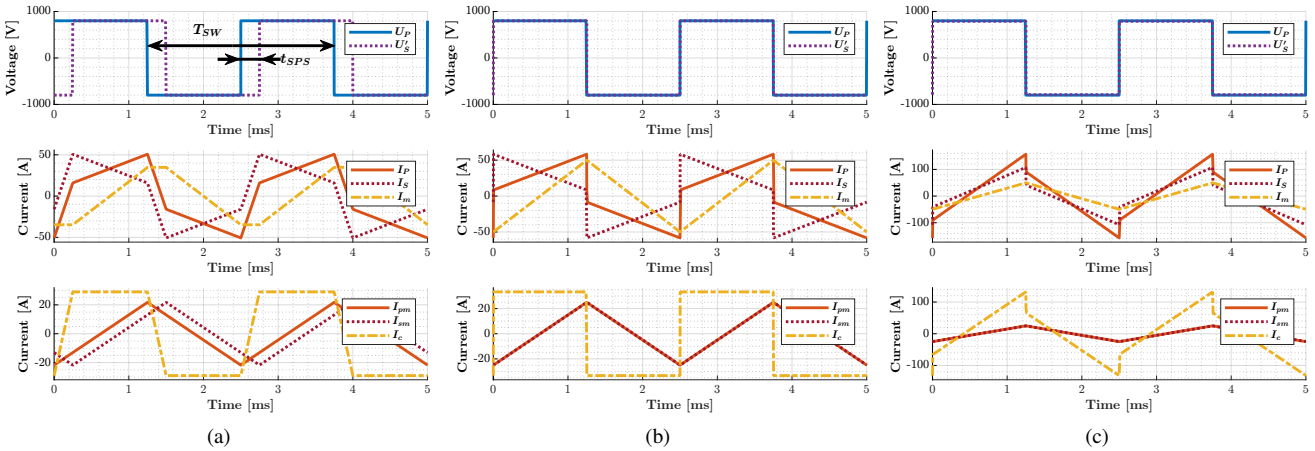

Fig. 2. DAB converter SPS control waveforms ($L_m = 10\,\text{mH}$, $U_{DCP} = 800\,\text{V}$, $L_s = L_{sp} = L'_{ss}$). (a) $U'_{DCS} = 800\,\text{V}$, $L_s = 3\,\text{mH}$; (b) $U'_{DCS} = 800\,\text{V}$, $L_s = 30\,\mu\text{H}$; (c) $U'_{DCS} = 790\,\text{V}$, $L_s = 30\,\mu\text{H}$.

In the following sections, a novel control technique called Ripple Current Control (RCC) is presented, which can mitigate unwanted ripple current during the operation of the DAB converter. It is achieved by an additional outer control loop, providing the ideal U'_{DCS} reference value for the rest of the cascaded controllers. The RCC allows the usage of transformers with a significantly smaller leakage inductance, which is required for the cost-effective improvement of transient response. By controlling ripple current amplitude, the converter efficiency and EMI performance can be improved, which are important factors in power conversion applications [16]. The proposed control method was tested in a hardware-in-the-loop (HIL) simulation and on a real converter.

In Section 2, equations are derived to demonstrate the connection between the ripple current and the voltage difference, revealing the main idea behind the proposed control technique. This is presented in Section 3. The test system and the RCC implementation details are introduced in Section 4. The HIL simulation environment, methodology, and results are presented in Section 5, which shows that the RCC behaves as intended. Finally, the proposed control was tested on the real hardware. The results are shown in Section 6.

2. Mathematical analysis of the current waveforms

To explain how does the ripple current can be controlled, a few equations are going to be derived for the transformer currents. The transformer is modeled with three inductors in a T network as shown in Figure 1. The equation system can be written in the s-domain as the following:

$$I_P(s) = \frac{1}{s}\frac{1}{L_{sp}}(U_P(s) - U_m(s)) \tag{1}$$

$$I'_S(s) = \frac{1}{s}\frac{1}{L'_{ss}}(U_m(s) - U'_S(s)) \tag{2}$$

$$I_m(s) = I_P(s) - I'_S(s) \tag{3}$$

$$U_m(s) = sL_m I_m(s) \tag{4}$$

Using (1)-(4), we can express I_P and I'_S as the function of the voltage and inductance values.

$$I_P(s) = \underbrace{\frac{1}{s}\frac{L_m}{k}(U_P(s) - U'_S(s))}_{I_c} + \underbrace{\frac{1}{s}\frac{L'_{ss}}{k}U_P(s)}_{I_{pm}} \tag{5}$$

$$I'_S(s) = \underbrace{\frac{1}{s}\frac{L_m}{k}(U_P(s) - U'_S(s))}_{I_c} - \underbrace{\frac{1}{s}\frac{L_{sp}}{k}U'_S(s)}_{I_{sm}} \tag{6}$$

$$k = L_m(L_{sp} + L'_{ss}) + L_{sp} + L'_{ss} \tag{7}$$

Based on (5) and (6), the primary and secondary current can be broken down to the sum of three current components. One of them is included in both equations, thus we can call it the common component (I_c), which is zero if $U_{DCP} = U'_{DCS}$. In this case two components remain. Using (3) we can see that these are the magnetizing current components flowing through L_{sp} and L'_{ss}, thus we can refer to them as I_{pm} and I_{sm} respectively. Note that these three current components are virtual yet essential to control the ripple current of the transformer as described in the next section.

3. Control of ripple current

If an SPS controlled DAB converter is in voltage balance ($U_{DCP} = U'_{DCS}$), I_c is zero between phase-shift actions, as $U_P - U_S = 0$. However, based on (5) and (6), I_P and I'_S will change and cause ripple current as shown in Figure 2 (b). If $U_P \neq U'_S$, then I_c plays a role in the resulting ripple current. If the voltage difference is high, I_c can significantly increase the overall ripple current (see an example in Figure 2 (c)).

The magnetizing current is inevitable. It must be supplied from the primary or the secondary side or both. Any higher ripple current should be avoided to limit the current stress on the switching devices. Fortunately, I_c can be controlled by changing the voltage difference. Let q denote the secondary magnetizing current component proportion to the total. If we want to force the magnetizing current to the secondary side ($q = 1$), I_c must be equal to $-I_{pm}$, thus canceling I_{pm} out in (5). The magnetizing current can be sup-

plied similarly from the primary side only ($I_c = I_{sm}$). All possible magnetizing current distribution can be expressed in one equation using q.

$$I_c = -qI_{pm} + (1-q)I_{sm} \tag{8}$$

The required voltage difference is expressed by substituting I_c, I_{pm}, I_{sm} from (5) and (6) into (8).

$$\frac{1}{s}\frac{L_m}{k}\left(U_P - U_S'\right) = -q\frac{1}{s}\frac{L_{ss}'}{k}U_P + (1-q)\frac{1}{s}\frac{L_{sp}}{k}U_S' \tag{9}$$

By multiplying both sides of the equation with $s \cdot k$, the equation can be rearranged to express the transformer voltage ratio as a function of q.

$$\frac{U_S'}{U_P} = \frac{L_m + qL_{ss}'}{L_m + (1-q)L_{sp}} \tag{10}$$

If the stray parameters (L_{sp} and L_{ss}') are considerably smaller than L_m, a few volts of difference could result in a completely different ripple current amplitude.

This can also be used to our advantage; controlling the ripple current by changing the voltage difference. In a DAB converter, the transformer's primary and secondary side voltage amplitude depends on the primary and secondary side DC voltage levels. In other words, the ripple current level can be controlled by changing the DC voltage ratio.

4. Application

An example application is used to illustrate, test, and validate the proposed ripple current control. This 360 kW DAB converter is part of a high-power test laboratory (Figure 3). Its main purpose is to provide galvanic isolation between the primary and secondary sides, keeping a constant voltage ratio. The transformer has multiple windings, which provide six different turns ratio, varying between 0.5-1.5. Before the converter starts up, the required configuration can be selected with contactors. The resulting transformer parameters are summarized in Table I. The nominal frequency of the transformer, thus the switching frequency, is 400 Hz. The primary voltage can vary between 600 V-800 V. The bridges are built from liquid-cooled 1000 A/1700 V IGBT modules. The maximum output current is limited to 750 A. Transformer and DC currents (I_{DCP}, I_{DCS}, I_P, I_S) are measured with fast Hall-effect sensors to allow current control. The two bridges are controlled with a single TMS320F28075 DSP.

In most applications, U_P and U_S are not measured directly in order to avoid common-mode voltage issues in the analog circuits. Instead, the DC link capacitor voltage is used to achieve the desired voltage ratio. Precise voltage measurement is needed to avoid large ripple currents as the voltage ratio difference required for $q = 1$ or $q = 0$ is lower than 1 % (see in Table I). In addition, the transformer terminal voltage is slightly different from the measured DC link voltage during operation due to the wiring resistance and the voltage drop on the IGBT modules, which are load and temperature-dependent parameters. To avoid dealing with voltage measurement errors and to regulate the ripple current of the transformer to the desired level, a suitable digital control loop is proposed, which can be seen in Figure 4 (a).

Table I. – The available transformer configurations and parameters

Turns ratio (n)	L_{sp}	L_{ss}'	L_m	$1-\frac{U_S'}{U_P}$	R_P	R_m	R_S'
1.5 and 0.75	$17.0\mu H$	$17.0\mu H$	$5.0mH$	$\pm 0.34\%$	$4.8m\Omega$	130Ω	$2.7m\Omega$
1.2 and 0.60	$25.3\mu H$	$25.3\mu H$	$7.9mH$	$\pm 0.32\%$	$6.1m\Omega$	190Ω	$4.2m\Omega$
1.0 and 0.50	$28.2\mu H$	$28.2\mu H$	$11.1mH$	$\pm 0.25\%$	$7.4m\Omega$	273Ω	$6.0m\Omega$

(a) (b) (c)

Fig. 3. The 360 kW DAB converter used for the experiments.
(a) Primary bridge and capacitors, (b) transformer, control, and contactors, (c) secondary bridge and capacitors.

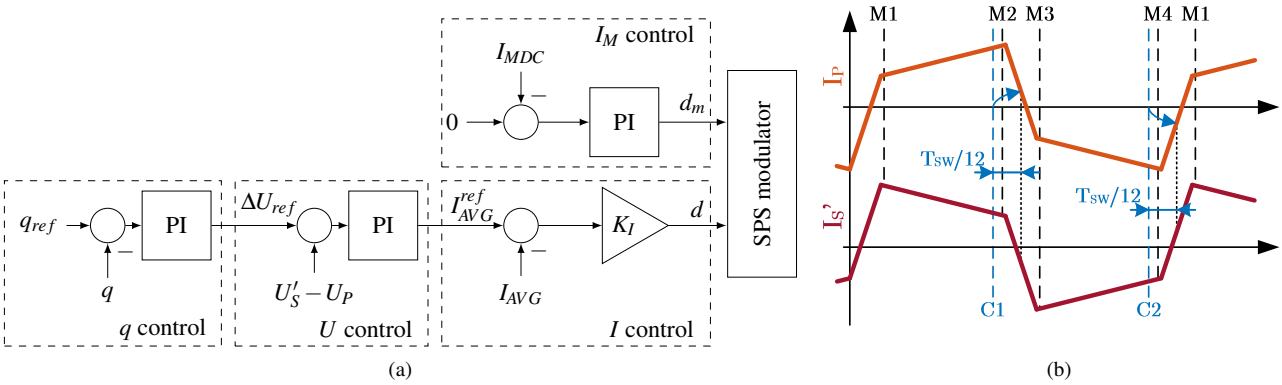

Fig. 4. Ripple current (a) control loop and (b) sampling points.
C1, C2: voltage and current sampling, control loop execution; M1-M4: current sampling for q calculation.

The control logic is executed twice in one switching period as shown in Figure 4 (b). At the C1 and C2 points, the transformer currents and the DC voltages are sampled to calculate I_{AVG}, I_{MDC}, U_P, and U'_S for the control loop. Once the conversion is complete, the control logic is executed, and the PWM peripheral compare registers are updated based on the controller output values. The q value is calculated at C1 and C2. However, the required transformer currents are sampled at M3, M4 and M1, M2, respectively. The exact timing of the M1-M4 sampling points is calculated from the updated PWM peripheral compare register values. Thus, the sampling always happens earlier than the first switching action and later than the last one.

The I_M controller keeps the DC component of the transformer magnetizing current near zero to avoid saturation. I_{MDC} can be calculated by (11) from the sampled transformer currents. The controller output (d_m) is used to change the 50 % duty cycle of the primary and secondary voltage waveforms.

$$I_{MDC} = \frac{(I_{PC2} - I'_{SC2}) + (I_{PC1} - I'_{SC1})}{2} \tag{11}$$

The current controller calculates the duty cycle for the required average current. I_{AVG} is calculated differently at C1 and C2 as shown in (12) and (13). The voltage controller produces the average current reference to keep the voltage difference at the required level.

$$I_{AVGC1} = \frac{(I_{PC1} + I'_{SC1})}{2} \tag{12}$$

$$I_{AVGC2} = -\frac{(I_{PC2} + I'_{SC2})}{2} \tag{13}$$

The current controller proportional coefficient can be calculated based on the transformer parameters and the voltage measurements as shown in (14).

$$K_I = \frac{L_{sp} + L'_{ss}}{T_{sw}(U_P + U'_S)} \tag{14}$$

The voltage controller regulates the primary and secondary side voltage difference to the requested value. The PI controller parameters were chosen to achieve the fastest disturbance response without an overshoot as described in [15].

The transformer ripple current is controlled by the q controller. The feedback is calculated differently in M2 and M4 as shown in (15) and (16). The idea is to measure the change in the primary and secondary current between M1-M2 and M3-M4 points and based on that, modify the voltage difference reference to achieve the needed ripple proportion.

$$q_{M2} = \frac{(I'_{SM1} - I'_{SM2})}{(I_{PM2} - I_{PM1}) + (I'_{SM1} - I'_{SM2})} \tag{15}$$

$$q_{M4} = \frac{(I'_{SM4} - I'_{SM3})}{(I_{PM3} - I_{PM4}) + (I'_{SM4} - I'_{SM3})} \tag{16}$$

This PI controller was tuned to be slow as only the steady-state behavior was important in this experiment. $P = 0.05$ and $I = 0.1$ parameters were selected for the test application based on empirical tuning.

The control algorithm does not use equation (10) because, usually, the inductance parameters of the transformer are not only unknown but vary during operation. The stray inductances are especially hard to measure individually. In most applications, only their sum is known. The PI controller integrator learns these unknown system parameters during operation. If the transformer inductance values are roughly known, then the required ΔU_{ref} voltage difference can be approximated with (10) and fed forward in the q controller to achieve a better transient response.

The suggested q_{ref} selection strategy is to use 0.5 if the converter load is light. In high load conditions, the magnetizing current should be forced to the higher voltage side ($q = 0$ or $q = 1$). This way the peak current on the lower voltage side will be smaller, which reduces thermal and current stress on the semiconductors.

5. Simulation

The proposed control algorithm was tested in hardware-in-the-loop (HIL) simulation. The main circuit model was running on a Digilent Zybo Z7 (Zynq-7000 SoC) development board. The control loop was implemented on a Texas Instruments TMS320F28075 DSP. A photo of the utilized HIL system can be seen in Figure 6.

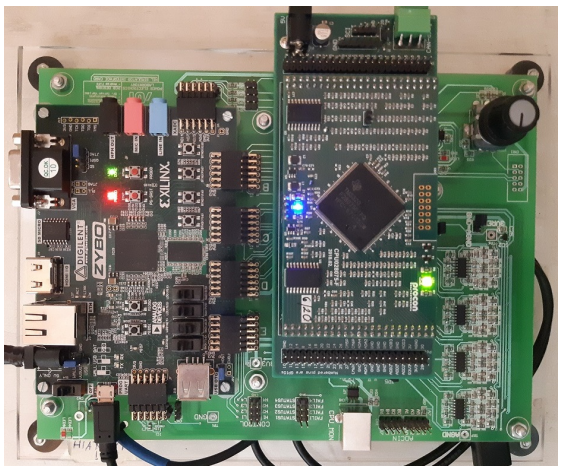

Fig. 6. The devices used for the real-time HIL simulation.
A Digilent Zybo Z7 (left) and a Texas Instruments TMS320F28075 DSP-based controller card (right).

A. *Implementation*

The main circuit model was created based on Figure 5 in MATLAB Simulink environment. Compared to Figure 1, additional circuit elements are taken into account, such as the transformer winding and core loss resistance, primary side bus impedance. The exact parameter values used in the simulation are shown in Table I, which are based on measurements. The primary side capacitor (C_P) has 20.4 mF of capacitance, the secondary side one (C_S) has 13.6 mF. The primary side busbar is modeled with a 200 nH and 10 mΩ LR circuit.

The four phase-legs of the inverters were modeled with the switching function method [17]. The diode forward voltage and the IGBT saturation voltage were not included in the model. The effective switching dead time has a significant effect on the operation of most switched mode power converters [18]. This is extremely true in this DAB converter as the required t_{SPS} phase-shift duration and the effective dead time is in the same order of magnitude. These effects were taken into consideration with a constant 3 µs turn-off and 2 µs turn-on delay for each IGBT. These values were selected based on measurements of the real hardware, including the IGBT switching characteristics, PWM signal propagation delay, and gate driver delay. The rest of the main circuit was modeled based on the circuit's differential equations as described in [17].

The next step was to discretize the model as the FPGA can only run the simulation with a fixed timestep. This means that a discrete-time model is needed in the Simulink environment, from which MATLAB's HDL Coder package can generate the Verilog source code for the FPGA. The continuous-time integrators were replaced with their forward Euler discrete equivalent ($z^{-1}/(1-z^{-1})$). After this, the model was compiled to the Zynq-7000 SoC-based development board, which can run the discrete model of the main circuit with 40 ns timestep. The simulated current and voltage values were available as analog outputs on the development board, the same way as on the real DAB converter. The analog signals were produced with Σ-Δ DACs in the FPGA with external RC low-pass filters.

For the control implementation, a Texas Instruments TMS320F28075 DSP-based controller card was used, the same as in the real converter (see in Figure 3 (b)). The RCC algorithm was written in the C programming language. The PI controllers were implemented with discrete equivalents as described in [15]. In the PWM peripheral, the inserted dead time was set to 3.7 µs. The effect of the switch delays (effective dead time) was compensated with an adaptive method as presented in [19]. The DSP read the analog values, ran the control, and gave out the PWM signals without knowing that the main circuit was only simulated.

B. *Methodology*

Our main goal with the simulation was to prove that the ripple current control algorithm is functional in multiple operation points. The simulation was done with both power flow directions, multiple turns ratios, and q_{ref} settings, even with disabled ripple current control to illustrate its necessity. In each test case, a constant secondary side current was applied as a load to draw $\pm 300A$ from the $650V$ primary side voltage source.

A debugging tool (ChipScope Pro Analyzer) was used to gather data from the SoC once the load change transients were settled. This way, the simulated values can be observed without any measurement errors involved. The used sampling time was 3.08 ms, and the sampling buffers held 4096 values, resulting in approximately five switching periods of data.

The samples were further processed with MATLAB to determine the peak-to-peak ripple current between each

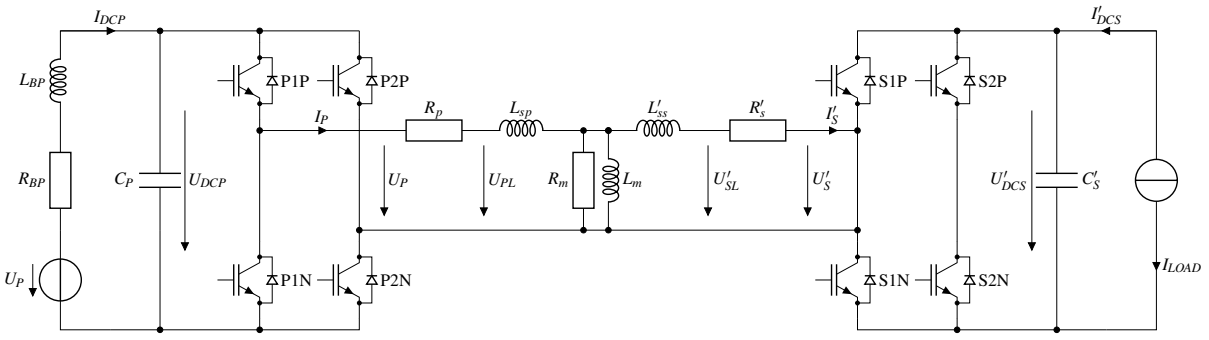

Fig. 5. The implemented main circuit model in the HIL simulation.

switching action. As five switching periods were recorded, the average of these values was calculated for each operation point. For comparison purposes, the ripple as a percentage of the average current was calculated between each switching action.

C. Results

Table II shows the summary of the simulation result data. When the RCC is turned off ($\Delta U_{ref} = 0\,\mathrm{V}$), the current ripple is high and distributed unevenly in all operating points. It can be extremely large, as shown in Figure 7. In such case, the I_c component of the current is much higher than the magnetizing components. This high current level is caused by voltage measurement errors (FPGA DAC and DSP ADC offset and non-linearity) and the simulated transformer resistance. Thus, the voltages at the transformer leakage inductances (see U_{PL} and U'_{SL} in Figure 5) are not equal after a switching action, even if the voltage controller runs properly and keeps the measured DC voltages at the requested equal level.

With $q_{ref} = 0.5$ settings, the RCC successfully distributes the magnetizing current evenly to both sides by detecting the current ripple inequality and adjusting the voltage controller reference to compensate the voltage drop across the transformer resistance and the voltage measurement errors. The control behaves as expected with the $q_{ref} = 0$ and $q_{ref} = 1$ reference value, the ripple is mainly supplied from either the primary or secondary side as requested. Based on these observations, the ripple current control is functioning as intended. There are no glitches or unwanted artifacts in the waveforms. The peak current stress on the IGBTs is reduced using the proposed control technique.

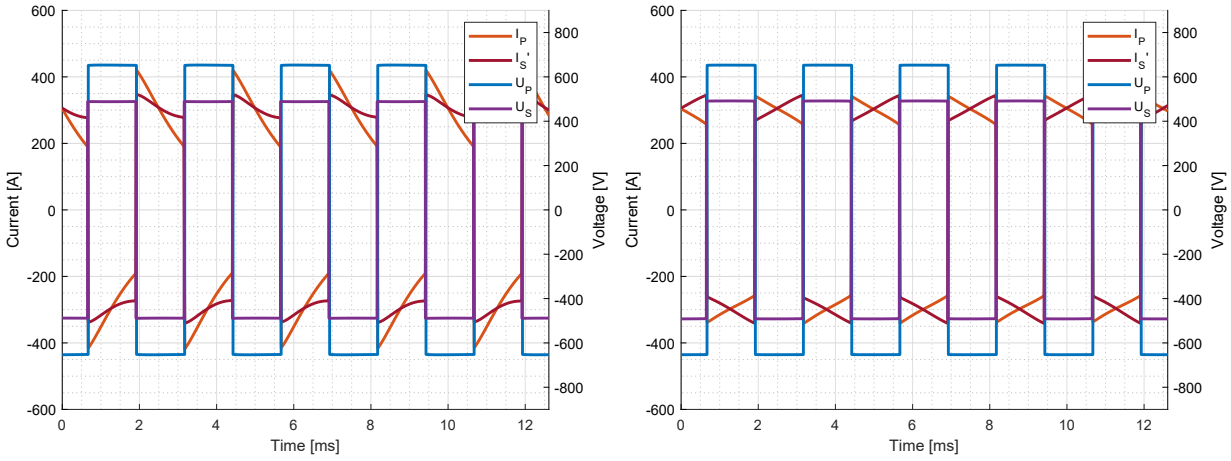

Fig. 7. Simulation result with and without the proposed ripple current control ($n = 0.8$, $I_P = -300\,\mathrm{A}$).
(a) RCC disabled, (b) RCC enabled with $q = 0.5$ (magnetizing current provided equally from both sides)

Table II. – HIL simulation results for various ripple current control reference values

q_{ref}	I_{DCP}	n	ΔI_{TRP}		$\Delta I'_{TRS}$	
OFF	300A	1.5	68.0A	21.9%	226.4A	73.9%
		1.2	10.8A	3.5%	111.4A	36.2%
		1	9.0A	2.9%	79.0A	25.6%
		0.75	53.3A	17.2%	106.5A	34.9%
		0.6	9.8A	3.1%	91.5A	29.7%
		0.5	31.8A	10.2%	103.7A	33.6%
	-300A	1.5	103.2A	34.5%	58.5A	19.3%
		1.2	145.7A	48.3%	44.8A	14.7%
		1	173.9A	57.4%	100.9A	33.1%
		0.75	227.1A	76.2%	66.3A	21.9%
		0.6	173.8A	57.6%	72.2A	23.7%
		0.5	166.0A	54.8%	93.7A	30.7%
0.5	300A	1.5	77.8A	25.1%	81.4A	26.6%
		1.2	49.4A	15.9%	50.7A	16.5%
		1	33.3A	10.8%	38.1A	12.4%
		0.75	79.8A	25.7%	79.2A	25.9%
		0.6	49.4A	15.9%	51.0A	16.6%
		0.5	36.1A	11.6%	35.8A	11.6%
	-300A	1.5	81.0A	27.1%	80.7A	26.6%
		1.2	51.6A	17.1%	50.1A	16.4%
		1	36.3A	11.9%	36.6A	12.0%
		0.75	83.3A	27.9%	79.1A	26.1%
		0.6	51.4A	17.0%	51.0A	16.7%
		0.5	37.6A	12.4%	35.3A	11.5%

q_{ref}	I_{DCP}	n	ΔI_{TRP}		$\Delta I'_{TRS}$	
1	300A	1.5	2.6A	0.8%	159.4A	52.1%
		1.2	5.1A	1.6%	102.0A	33.1%
		1	4.3A	1.4%	70.5A	22.9%
		0.75	5.1A	1.7%	155.5A	50.9%
		0.6	4.9A	1.6%	99.5A	32.3%
		0.5	5.6A	1.8%	68.9A	22.4%
	-300A	1.5	4.4A	1.5%	162.2A	53.5%
		1.2	4.1A	1.3%	100.9A	33.0%
		1	3.5A	1.1%	72.4A	23.6%
		0.75	7.9A	2.7%	155.5A	51.1%
		0.6	7.3A	2.4%	99.7A	32.6%
		0.5	7.7A	2.5%	68.5A	22.3%
0	300A	1.5	155.8A	50.4%	8.8A	2.9%
		1.2	97.6A	31.5%	5.4A	1.8%
		1	68.5A	22.1%	4.6A	1.5%
		0.75	154.6A	49.9%	8.3A	2.7%
		0.6	98.5A	31.8%	5.8A	1.9%
		0.5	67.2A	21.7%	7.1A	2.3%
	-300A	1.5	160.7A	53.8%	4.9A	1.6%
		1.2	100.8A	33.4%	3.9A	1.3%
		1	73.7A	24.3%	4.3A	1.4%
		0.75	162.0A	54.3%	5.7A	1.9%
		0.6	101.5A	33.6%	2.7A	0.9%
		0.5	72.5A	23.8%	1.5A	0.5%

6. Experimental results

A. Environment and setup

The proposed RCC technique was tested on the real 360 kW DAB converter, which is part of the BME Modular Hybrid Drive System laboratory built-in converters (see in Figure 8 (a)). The probe arrangement is shown in Figure 8 (b).

The primary side current was measured with a Tektronix A6304XL 500 A AC/DC current probe. On the secondary side, we used the Tektronix TCP404XL for current measurement. Both have similar specs.

The primary and secondary transformer voltages (bridge output voltage) were measured with differential probes. A Rohde&Schwarz RT0-1004 oscilloscope was used to capture the voltage and current probe signals with a high sampling rate for a few switching periods.

B. Methodology

Various power converters were involved in the tests, which are built-in equipment of the laboratory. A high-power DC/DC converter was connected between the primary and secondary sides of the DAB converter to provide a constant 300 A or -300 A load on its output. This way, the power was circulating inside the laboratory. Due to the dissipation losses, a grid-connected AC/DC converter had to be used to keep the DAB converter primary side voltage at a constant 650 V level. With the available built-in converter configuration, we were only able to test with the $n = 1.2$ transformer ratio setting. As a result, the secondary side nominal voltage was 780 V.

The DAB converter was operated with different q_{ref} values and ± 300 A load current level to enable the comparison of simulation data. The transformer current and voltage were captured with 10 ns sampling time. A total of one million samples were collected for each oscilloscope channel, resulting in a 10 ms long time window.

The data was exported and further processed with MATLAB. On the signals, a moving average with 500 samples wide (5 µs) window was used to remove measurement noise. The secondary side current was reduced to the primary side level (divided by $n = 1.2$) to allow visual comparison of the current plots.

C. Results

The processed experimental waveforms are shown in Figure 9 for positive load current. The current ripple values were calculated as in Section 5 to enable direct comparison to the simulation results. The experimental data can be found in Table III.

When the RCC is turned off ($\Delta U_{ref} = 0$ V), the current ripple is higher compared to the simulation results. This is caused by voltage measurement errors in the hardware, such as voltage divider imperfections, amplifier gain, and offset errors, and additional resistance in the busbars, because the DC voltage is measured with the controlling DSP on the DC capacitors, not between the transformer leads. The ripple value is nearly equal to the average current, resulting in around 500 A peak primary transformer current, causing unwanted stress on the semiconductors and on the capacitors.

(a) (b)

Fig. 8. Measurement setup in the laboratory. (a) Location of the DAB converter, (b) probe arrangement.

Table III. – Experimental ripple current control results with $n = 1.2$ transformer ratio

q_{ref}	I_{DCP}	ΔI_{TRP}		$\Delta I'_{TRS}$	
OFF	300A	238.2A	71.90%	296.6A	90.70%
	-300A	246.1A	81.60%	181.9A	58.60%
0.5	300A	34.4A	10.20%	27.8A	8.40%
	-300A	31.9A	10.00%	37.5A	11.70%

q_{ref}	I_{DCP}	ΔI_{TRP}		$\Delta I'_{TRS}$	
1	300A	12.0A	3.60%	63.6A	19.20%
	-300A	10.2A	3.20%	65.4A	20.80%
0	300A	65.1A	19.30%	10.2A	3.10%
	-300A	67.5A	21.70%	16.0A	5.10%

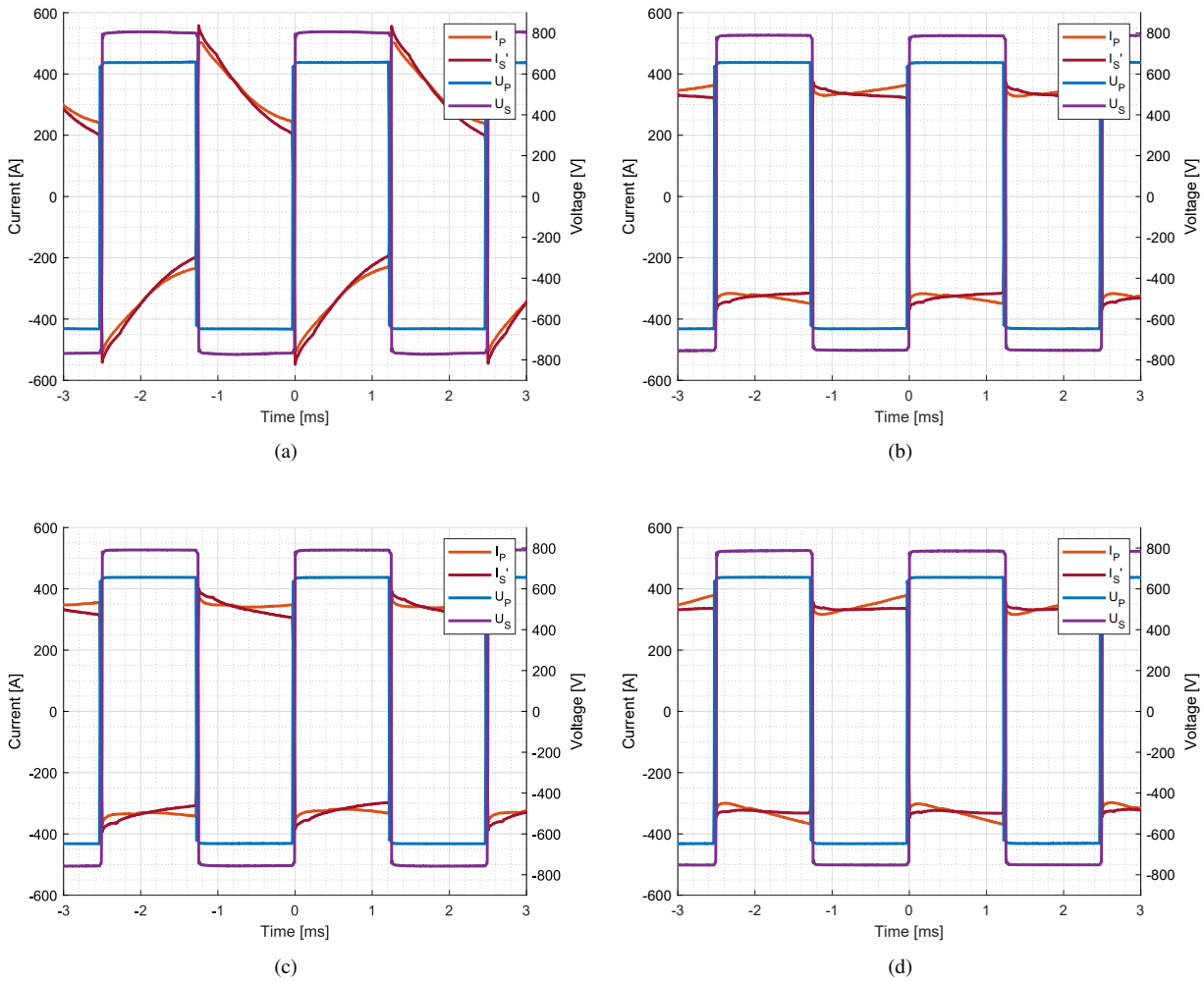

Fig. 9. Experimental results ($n = 1.2$). (a) q_{ref} = OFF, (b) $q_{ref} = 0.5$, (c) $q_{ref} = 1.0$, (d) $q_{ref} = 0.0$

By enabling the RCC with a 0.5 reference value, the ripple current is reduced and distributed evenly between the primary and the secondary side. A slight difference can be observed, but considering that the DSP current measurement range is $\pm 1000\,\mathrm{A}$ ($10\,\mathrm{A}$ difference is only $1\,\%$), a few amperes of error in the control is acceptable. When q_{ref} is set to 0 and 1, the ripple current is successfully forced to the secondary and the primary side as requested. Based on the measurements, the RCC works as intended without any issues.

7. Conclusion

In this paper, a new control scheme was proposed for single phase-shift dual active bridge converters to regulate the transformer's current ripple. Equations were derived showing the base idea of the control operation. The ripple current control algorithm was implemented on a DSP, then tested in a HIL simulation environment and in a real $360\,\mathrm{kW}$ DAB converter. The proposed control was able to regulate the ripple current of the transformer expectedly.

Using this controller, the excessive transformer ripple current, caused by voltage measurement errors, can be mitigated, reducing the current stress on the semiconductors and on the DC capacitors. In addition, the transformer magnetizing current can be forced to flow from the higher voltage side of the converter, resulting in less current stress on the lower voltage side, increasing the utilization of the semiconductor switches and decreasing conduction losses.

Acknowledgement

Supported by the ÚNKP-23-3-I-BME-27 New National Excellence Program of the Ministry for Culture and Innovation from the source of the National Research, Development and Innovation Fund.

This research was supported by the Ministry of Culture and Innovation and the National Research, Development and Innovation Office within the Cooperative Technologies National Laboratory of Hungary (Grant No. 2022-2.1.1-NL-2022-00012).

References

[1] P. Pradhan, I. Ahmad, D. Habibi, A. Aziz, B. Al-Hanahi, and M. A. S. Masoum, "Optimal sizing of energy storage

system to reduce impacts of transportation electrification on power distribution transformers integrated with photovoltaic," *IEEE Access*, vol. 9, pp. 144 687–144 698, 2021.

[2] D. Mishra, B. Singh, and B. K. Panigrahi, "Adaptive current control for a bidirectional interleaved ev charger with disturbance rejection," *IEEE Transactions on Industry Applications*, vol. 57, pp. 4080–4090, 2021.

[3] S. Shao, L. Chen, Z. Shan, F. Gao, H. Chen, D. Sha, and T. Dragičević, "Modeling and advanced control of dual-active-bridge dc-dc converters: A review," *IEEE Transactions on Power Electronics*, vol. 37, pp. 1524–1547, 2022.

[4] A. Chambayil and S. Chattopadhyay, "A dual active bridge converter with multiphase boost interfaces for single-stage bidirectional dc-ac conversion," *IEEE Transactions on Industry Applications*, vol. 57, pp. 2638–2653, 2021.

[5] R. W. A. A. DeDoncker, D. M. Divan, and M. H. Kheraluwala, "A three-phase soft-switched high-power-density dc/dc converter for high-power applications," *IEEE Transactions on Industry Applications*, vol. 27, no. 1, pp. 63–73, Jan. 1991.

[6] R. W. DeDoncker, M. H. Kheraluwala, and D. M. Divan, "Power conversion apparatus for dc/dc conversion using dual active bridges," US Patent US5 027 264A, 1991. [Online]. Available: https://patents.google.com/patent/US5027264A/en

[7] M. N. Kheraluwala, R. W. Gascoigne, D. M. Divan, and E. D. Baumann, "Performance characterization of a high-power dual active bridge dc-to-dc converter," *IEEE Transactions on Industry Applications*, vol. 28, no. 6, pp. 1294–1301, 1992.

[8] N. Noroozi, A. Emadi, and M. Narimani, "Performance evaluation of modulation techniques in single-phase dual active bridge converters," *IEEE Open Journal of the Industrial Electronics Society*, vol. 2, pp. 410–427, 2021.

[9] S. Guo, J. Su, J. Lai, and X. Yu, "Analysis and design of a wide-range soft-switching high-efficiency high-frequency-link inverter with dual-phase-shift modulation," *IEEE Transactions on Power Electronics*, vol. 33, pp. 7805–7820, 2018.

[10] S. M. Akbar, A. Hasan, A. J. Watson, and P. Wheeler, "Model predictive control with triple phase shift modulation for a dual active bridge dc-dc converter," *IEEE Access*, vol. 9, pp. 98 603–98 614, 2021.

[11] S. Chakraborty and S. Chattopadhyay, "A dual-active-bridge-based fully zvs hf-isolated inverter with low decoupling capacitance," *IEEE Transactions on Power Electronics*, vol. 35, pp. 2615–2628, 2020.

[12] H. Zhang and T. Isobe, "An improved charge-based method extended to estimating appropriate dead time for zero-voltage-switching analysis in dual-active-bridge converter," *Energies*, vol. 15, no. 671, p. 671, 01 2022.

[13] B. Cui, P. Xue, and X. Jiang, "Elimination of high frequency oscillation in dual active bridge converters by dv/dt optimization," *IEEE Access*, vol. 7, pp. 55 554–55 564, 2019.

[14] X. Zhang, F. Xiao, R. Wang, W. Kang, and B. Yang, "Modeling and design of high-power enhanced leakage-inductance-integrated medium-frequency transformers for dab converters," *Energies*, vol. 15, no. 1361, p. 1361, 02 2022.

[15] S. Veréb, A. Futó, Z. Sütő, A. Balogh, and I. Varjasi, "Continuous cross-period single phase shift control for dual active bridge converters," *Renewable Energy & Power Quality Journal (RE&PQJ)*, vol. 19, pp. 222–228, Sep. 2021.

[16] A. Futo, I. Varjasi, I. Vajk, and R. K. Jardan, "Analytical compensation of harmonics caused by 60° flat-top modulation," *IET Power Electronics*, vol. 12, no. 7, pp. 1763–1773, Jun. 2019.

[17] C. Batard, F. Poitiers, C. Millet, and N. Ginot, *MATLAB - A Fundamental Tool for Scientific Computing and Engineering Applications*. IntechOpen, 2012, vol. 1, ch. 3, pp. 43–68.

[18] A. Futó and I. Varjasi, "Compensation of discontinuous conduction in single phase grid connected pwm inverters." Wroclaw, Poland: IEEE, 2013, pp. 126–131.

[19] S. Veréb, A. Futó, Z. Sütő, A. Balogh, and I. Varjasi, "Adaptive dead time compensation for cross-period single phase shift control of dual active bridge converters," *Renewable Energy & Power Quality Journal (RE&PQJ)*, vol. 18, pp. 327–332, Jun. 2020.